An unexpectedly large count of trees in the West African Sahara and Sahel

https://doi.org/10.1038/s41586-020-2824-5

Received: 26 August 2019

Accepted: 9 September 2020

Published online: 14 October 2020

Check for updates

Martin Brandt[1,2]✉, Compton J. Tucker[3]✉, Ankit Kariryaa[2,4], Kjeld Rasmussen[1], Christin Abel[1], Jennifer Small[2,3], Jerome Chave[5], Laura Vang Rasmussen[1], Pierre Hiernaux[2,6], Abdoul Aziz Diouf[7], Laurent Kergoat[8], Ole Mertz[1], Christian Igel[9], Fabian Gieseke[9,10], Johannes Schöning[4], Sizhuo Li[1], Katherine Melocik[2,3], Jesse Meyer[2,3], Scott Sinno[2,3], Eric Romero[2,3], Erin Glennie[2,3], Amandine Montagu[11], Morgane Dendoncker[12] & Rasmus Fensholt[1]

A large proportion of dryland trees and shrubs (hereafter referred to collectively as trees) grow in isolation, without canopy closure. These non-forest trees have a crucial role in biodiversity, and provide ecosystem services such as carbon storage, food resources and shelter for humans and animals[1,2]. However, most public interest relating to trees is devoted to forests, and trees outside of forests are not well-documented[3]. Here we map the crown size of each tree more than 3 m^2 in size over a land area that spans 1.3 million km^2 in the West African Sahara, Sahel and sub-humid zone, using submetre-resolution satellite imagery and deep learning[4]. We detected over 1.8 billion individual trees (13.4 trees per hectare), with a median crown size of 12 m^2, along a rainfall gradient from 0 to 1,000 mm per year. The canopy cover increases from 0.1% (0.7 trees per hectare) in hyper-arid areas, through 1.6% (9.9 trees per hectare) in arid and 5.6% (30.1 trees per hectare) in semi-arid zones, to 13.3% (47 trees per hectare) in sub-humid areas. Although the overall canopy cover is low, the relatively high density of isolated trees challenges prevailing narratives about dryland desertification[5–7], and even the desert shows a surprisingly high tree density. Our assessment suggests a way to monitor trees outside of forests globally, and to explore their role in mitigating degradation, climate change and poverty.

Trees have long been a central element in environmental science and policy in Africa: threats of deforestation, looming desertification, and 'stop encroaching deserts' and 'plant a tree' campaigns have been on the front pages of newspapers for decades[5–7]. Most attention is devoted to forests, which are often defined as areas of more than 25% canopy closure[8]. However, trees from outside of forest areas (non-forest trees) support the livelihoods of a rapidly increasing population through the subsistence use of products such as wood (for construction or fuel), food[9], fodder[10] and medicinal plants; through the cash income obtained from the sale of products[11]; and through ecological benefits such as protection against hazards (for example, erosion), soil improvement, water and nutrient cycling as well as pollination, which—in turn—improves agricultural productivity[1,10,12]. Moreover, trees in arid biomes are an essential factor for the survival and biodiversity of flora and fauna[13]. Finally, trees in farmlands, savannahs and deserts constitute an important—but very variable—carbon pool[14], and affect the climate by lowering the albedo, by altering aerodynamic roughness and through transpiration[1]. As non-forest trees are becoming increasingly recognized in environmental initiatives across Africa[15], there is a growing interest in consistently measuring and monitoring trees outside of forests at the level of single trees.

However, whereas the monitoring of forests has been carried out on a routine basis[8,16], attempts to quantify the density of trees outside of forests have been limited to small sample sizes[15,17–19] or local field surveys[15]. This is because of the scattered nature of dryland trees, which limits assessments based on commonly available satellite technologies (at a resolution of 10 to 30 m) to the canopy coverage per area, which leaves a blind spot with respect to the number, location and size of isolated trees[19–21]. The limited attention devoted to the quantification of individual trees in drylands has led to misinterpretations of the extent of canopy cover, and to confusion related to the definition of canopy cover (that is, the characteristics of woody plants included in calculations of 'coverage'). Products designed to assess global tree cover are poorly designed to quantify tree cover in drylands[22], which has resulted in the prevailing view that dryland areas such as the Sahara or Sahel are largely free of trees[15,16].

Here we present a wall-to-wall identification of non-forest trees (defined as woody plants with a crown size over 3 m^2) in the West African Sahara, Sahel and sub-humid zone, covering a rainfall gradient from hyper-arid (rainfall of 0–150 mm yr^{-1}), arid (rainfall of 150–300 mm yr^{-1}), semi-arid (rainfall of 300–600 mm yr^{-1}) to sub-humid (rainfall

[1]Department of Geosciences and Natural Resource Management, University of Copenhagen, Copenhagen, Denmark. [2]Science Systems and Applications Inc., NASA Goddard Space Flight Center, Greenbelt, MD, USA. [3]NASA Goddard Space Flight Center, Greenbelt, MD, USA. [4]HCI Group, University of Bremen, Bremen, Germany. [5]Laboratoire Evolution and Diversité Biologique, CNRS, UPS, IRD, Université Paul Sabatier, Toulouse, France. [6]Pastoralisme Conseil, Caylus, France. [7]Centre de Suivi Ecologique, Dakar, Senegal. [8]Geosciences Environnement Toulouse (GET), Observatoire Midi-Pyrénées, UMR 5563 (CNRS/UPS/IRD/CNES), Toulouse, France. [9]Department of Computer Science (DIKU), University of Copenhagen, Copenhagen, Denmark. [10]Department of Information Systems, University of Münster, Münster, Germany. [11]Département de Géosciences, Ecole Normale Supérieure, Paris, France. [12]Earth and Life Institute, Environmental Sciences, Université Catholique de Louvain, Louvain-la-Neuve, Belgium. ✉e-mail: mabr@ign.ku.dk; compton.j.tucker@nasa.gov

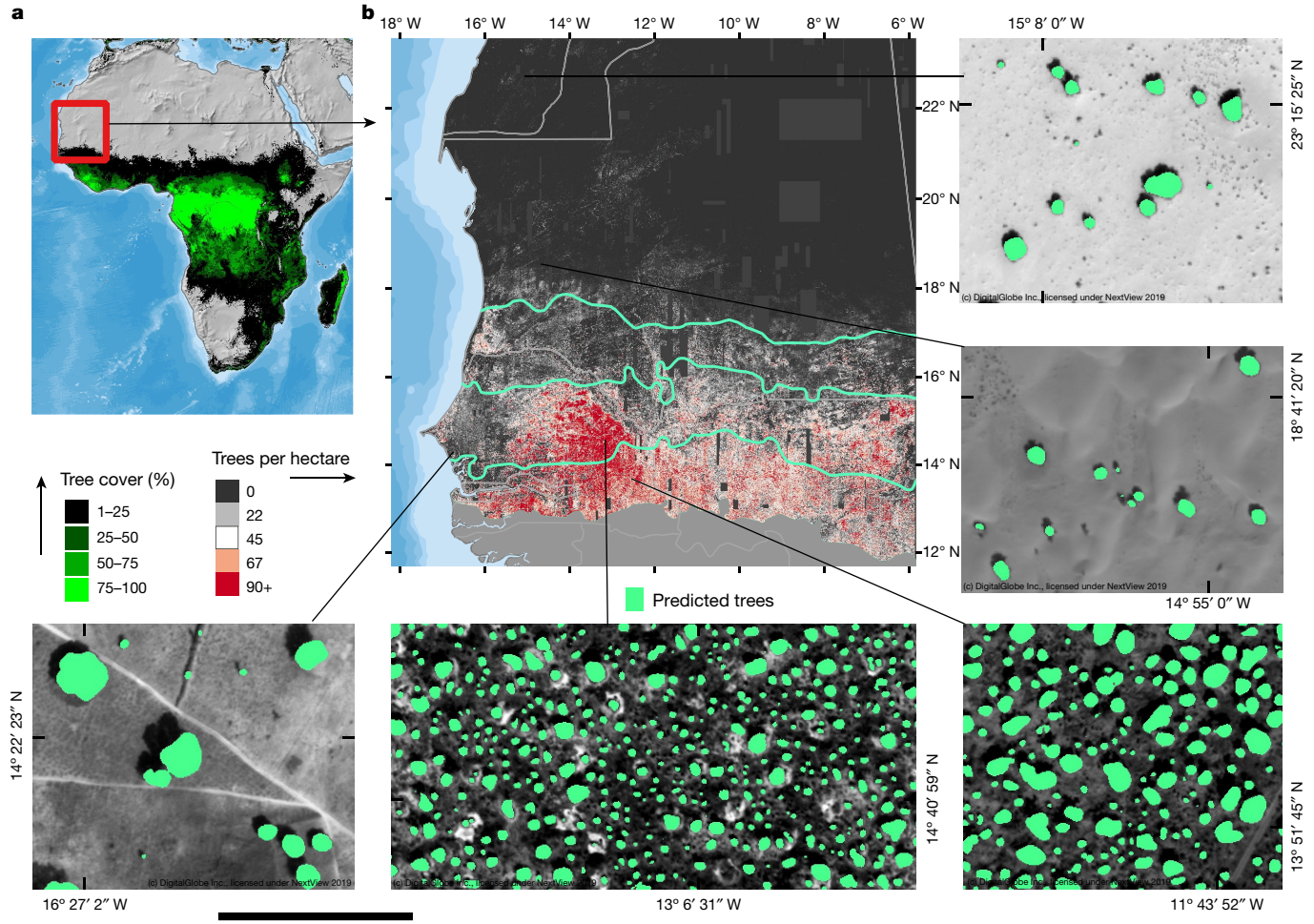

Fig. 1 | Mapping trees using deep learning. a, Forests in a previously published global tree-cover map[8] are defined as more than 25% canopy closure of trees taller than 5 m. This definition does not apply in most dryland areas, as in these regions trees grow mostly as isolated plants. This study mapped all trees (>3-m^2 crown size) in the red rectangle using deep learning applied to submetre-resolution satellite imagery. **b**, The density of trees per hectare along the rainfall gradient (0–1,000 mm yr^{-1}), derived from 1,837,565,501 trees. The cyan lines are the 150-, 300-, 600- and 1,000-mm-per-yr rainfall isohyets (mean 1982–2017), increasing from north to south. Illustrations show tree crowns mapped by the model. Scale bar, 100 m. Imagery 2019 © DigitalGlobe, Inc. under NextView License.

of 600–1,000 mm yr^{-1}) areas. We split the crown sizes into shrubs (3–15 m^2), small trees (15–50 m^2) and large trees (50–200 m^2), as well as very large trees and clumped canopies that form thickets or forests (over 200 m^2). The mapping of woody plants at the level of single trees was achieved by the use of satellite data at very high spatial resolution (0.5 m) from DigitalGlobe satellites, combined with modern machine-learning techniques. This satellite imagery, provided under the NextView licence, enables the introduction of variables that go beyond canopy cover at large spatial scales, which opens up perspectives for research on the human–environment nexus in drylands. We produced panchromatic and pansharpened normalized difference vegetation index (NVDI) datasets (both at 0.5-m spatial resolution), from 11,128 multispectral images from the GeoEye-1, WorldView-2, WorldView-3 and QuickBird-2 satellites. Here we assess tree density (number of trees per hectare) and the crown size of each individual tree. We further show how tree crown sizes, density and canopy cover are associated with rainfall and land use.

Our automatic tree detection framework is based on deep-learning techniques[4,23]. We make use of fully convolutional networks as one of the key algorithmic building blocks[24] (Methods). We trained a model with 89,899 manually delineated tree crowns on 0.5-m-resolution satellite imagery across a wide range of environmental conditions. We found that this model showed a high agreement between the manual annotations in the test data and the predicted results (Extended Data Figs. 1, 2). We used the visibility of a shadow and a minimum crown size of 3 m^2 as criteria for trees to be included in the assessment, which excludes small bushes that are difficult to separate from perennial grass tussocks. The disaggregation of clumped trees was achieved by giving the spaces between crowns a larger weight than other spaces during the learning process of the model (Extended Data Fig. 3). The result was the identification of more than 1.8 billion individual trees over about 1.3 million km^2 along a north–south rainfall gradient from 0 to 1,000 mm of rainfall per year (Fig. 1, Extended Data Fig. 4). We mapped the density, crown size and cover of these trees (Fig. 2, Extended Data Figs. 5, 6). Owing to the absence of closed canopies, most parts of this area have been mapped as 0% tree cover in previous assessments[8,20] (Fig. 1a, Extended Data Fig. 7a).

Our results show that tree density and coverage develop along the rainfall gradient (Fig. 3) from very sparse in the hyper-arid Sahara Desert in the north (0.7 ± 2.6 (mean ± s.d.) trees per hectare, and 0.1 ± 4% canopy cover), through scattered trees in arid (on average 9.9 ± 13.2 trees per hectare, and 1.6 ± 2.9% cover) and semi-arid (on average 30.1 ± 29.0 trees per hectare, and 5.6 ± 5.9% cover) lands, into denser patterns in the sub-humid south (on average 47 ± 30 trees per hectare, and 13.3 ± 9.4% cover). Trees with a crown size of 3–15 m^2 account for the majority of the density, but contribute only a little to the overall canopy cover. Small

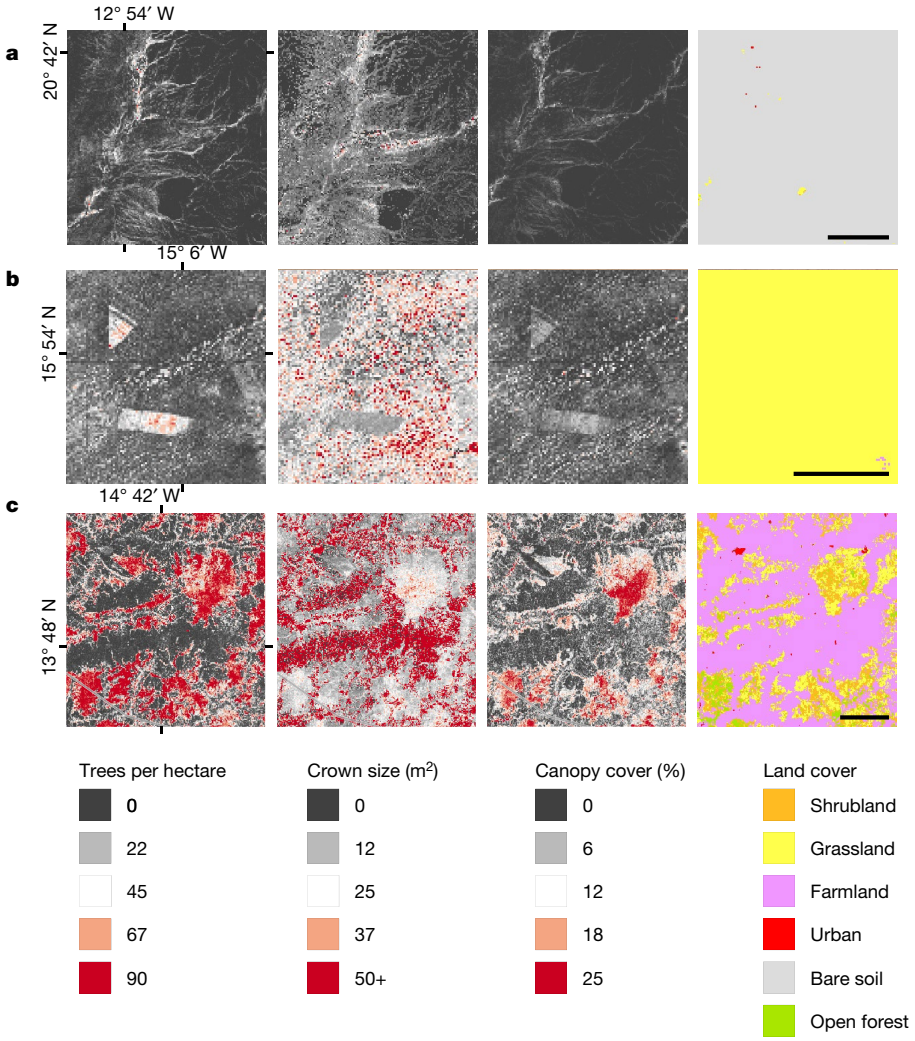

Fig. 2 | Examples of tree density, crown size and canopy cover. a, Trees in the Sahara Desert are abundant within ancient valleys, but the overall canopy cover is low. The high concentration in the western part of the image is the settlement of Atar (Mauritania). Scale bar, 5 km. **b**, Tree plantations in Senegal are part of the 'great green wall' and show a high density of small trees, but are hardly visible in the canopy-cover map. Scale bar, 5 km. **c**, Tree density and canopy cover are high in uncultivated areas, but are low in farmlands that are otherwise characterized by large crown sizes. Scale bar, 10 km. The maps are 1-ha grids counting the number of trees >3 m^2 per ha (density), their mean crown size and the area covered by trees (canopy cover). The land cover is derived from a previous publication[26].

crowns dominate low-rainfall zones; beyond 150- and 300-mm-per-year rainfall, larger crown sizes appear and gradually increase in density to make up large parts of the coverage (Fig. 3a), while the smaller crown-size class (3–15 m^2) decreases in density in the transition between the semi-arid and sub-humid zone. On average, canopy cover and tree density on sandy soils increase only weakly with rainfall, which suggests that the observed latitudinal increases (Fig. 1b) are closely related to the increasing dominance of non-sandy soils in the sub-humid zone (Fig. 3c, f, Extended Data Fig. 4b). The peak in both tree density and cover observed at around 400-mm-per-year rainfall reflects the managed agroforestry parklands in the semi-arid Sahel[21].

Canopies larger than 200 m^2 are very large individual trees or clumped crowns that could not be separated (Extended Data Fig. 6d), building thickets or forests[8]. The contribution of this class to the canopy cover is 6% (Fig. 3a), which means that accounting only for large patches of vegetation in canopy-cover assessments severely underestimates the total density and canopy cover. Figure 4 illustrates the distribution of the crown sizes (converted to crown diameter) within the different rainfall zones. Mean crown diameter consistently increases from the hyper-arid to the sub-humid rainfall zone, with a steeper slope as aridity increases. The crown diameters are exponentially distributed for each rainfall zone, which was confirmed by field data (Extended Data Fig. 7b, c). These results comply with tree demographic models that have both growth and mortality rates being independent of stem size (equation 2 in ref. [25]). By extrapolating the exponential model to crown size values of less than 3 m^2 (which were not mapped in our study), we estimate that 16–20% of the trees are in the 1–3-m^2 crown-size range. The crown diameter of trees in farmlands and urban areas is relatively independent of rainfall, and is generally larger compared to all sampled trees (Fig. 4b). This is visualized in Fig. 2c, which shows that trees with large crown sizes are located mainly in farmlands—albeit at a strongly reduced density compared to savannahs. The proportion of trees located in farmland and urban areas is highest in the semi-arid zone (13%), followed by the sub-humid (11%), arid (2%) and hyper-arid zones (0.1%).

Studies often disagree on definitions for woody plants, crown cover and forests, which leads to misinterpretations and a continuing uncertainty as to the number and size of trees in savannah regions[8,19,20]. Our study provides evidence to consider in this debate. The wall-to-wall assessment of crown sizes larger than 3 m^2 helps to

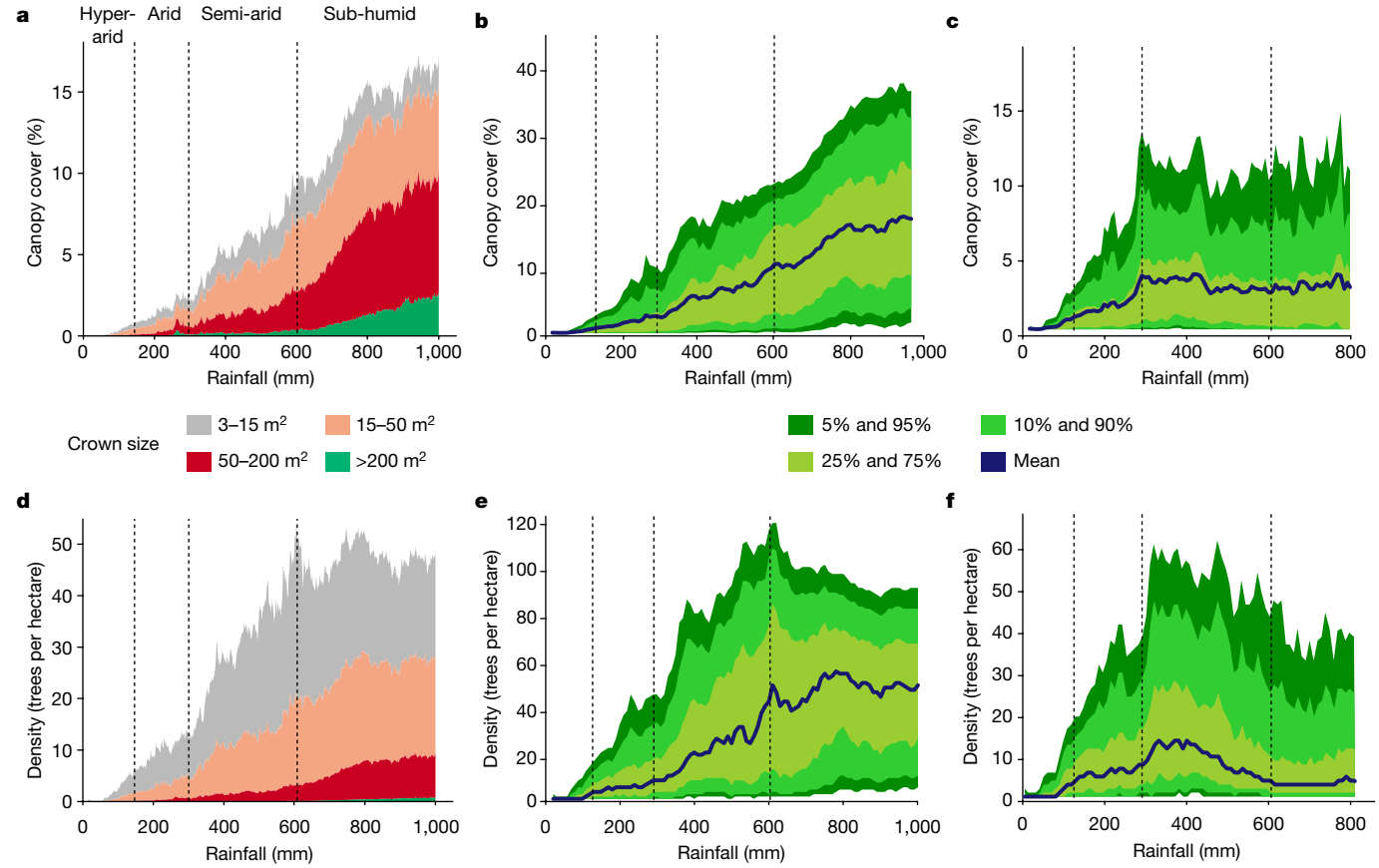

Fig. 3 | Cover and density of individual trees. a, The stacked contribution of the crown size classes to canopy cover is shown along the rainfall gradient (1-mm steps). **b**, Canopy cover in relation to annual rainfall (10-mm steps). **c**, As in **b**, but for sandy soils (>70% sand content) and up to 800-mm rainfall (owing to low coverage of sandy areas beyond this threshold). **d**, Tree density along the rainfall gradient (1-mm steps), stacked into crown size classes. **e**, Tree density along the rainfall gradient (10-mm steps). **f**, As in **e**, but for sandy soils. All statistics were derived from 1,837,565,501 trees (**a**, **b**, **d**, **e**) or 363,238,952 trees on sandy soils (**c**, **f**). The stacked total cover in **a**, **d** is equal to the mean lines in **b**, **e**. Vertical dotted lines indicate divisions between hyper-arid, arid, semi-arid and sub-humid zones, as labelled in **a**. Green shading represents confidence interval, as indicated in the key.

resolve controversies over the number of trees and the extent of canopy cover in drylands. Moreover, we were able to assign crowns to individual trees, and therefore map hundreds of millions of trees over hyper-arid, arid and semi-arid regions, which are areas with a relatively low canopy cover that have previously been classified as bare soil and desert[26]. Our results elucidate how widely used definitions of tree cover[8,20] are missing most of the trees and tree cover in these regions, because they are not designed to include isolated, non-forest trees. As our assessment neither includes trees with a canopy of less than 3 m^2 nor overlapped trees, the total number of trees is higher than reported here. One of the few previous studies[17] to have assessed trees as individuals for selected sites in African savannahs found similar patterns, but generally higher numbers of trees, than reported here. The only available large-scale assessment specifically designed to assess tree coverage in drylands used a systematic area-based sampling approach, and manual assessment of canopy cover[19]. We found that this analysis shows a low relationship with our results ($r^2 = 0.28$) (Extended Data Fig. 7d). A locally calibrated map using radar and NDVI time-series data displays a higher correlation with our results ($r^2 = 0.5$)[21], but—unlike the method we propose here—these previous methods do not produce fractional cover maps that correctly account for isolated trees.

We have shown that deep learning combined with very-high-spatial-resolution satellite imagery collectively represents a disruptive technology that delivers excellent models for detecting isolated trees over large areas. We found that the transferability of the model across regions can be low; this study had to use a very large number of training samples to achieve a high quality across landscapes. Training samples also had to cover a range of different satellite images: acquisition dates, dust, clouds, burned areas, solar zenith and viewing angle, off-nadir, sensor systems and image boundaries all affect the visibility of tree crowns. All of these variations need to be taken into account when training the model, which requires a vast amount of training data and makes training time-consuming. This currently challenges the use of deep learning for large-scale analyses of satellite images. Although accuracy assessments with independent satellite and field data are in excellent agreement with the predictions of our model (Extended Data Figs. 1, 2, Methods), the effects of the above-mentioned variability can be observed in practice (Extended Data Table 1). The use of mosaics that merge different sensors and dates introduces uncertainty, particularly because leaf density and the shape of the tree crowns vary from season to season. In the future, it is possible that satellite data at submetre resolution will be available at a temporal frequency that is sufficient to derive seamless mosaics, which would remove a source of bias from our method (Extended Data Fig. 8).

Combined with existing and future fieldwork, our assessment lays the foundation for a comprehensive database that contains information on all individual trees outside of forests. This will constitute a robust basis for understanding dryland ecosystems and the role of human agency and climate change in the distribution of dryland trees. Such information is crucial to understanding how the presence of trees influences agricultural yields and diversity, crop nutritional content[27], household food and nutrition security[28,29], and household wealth status.

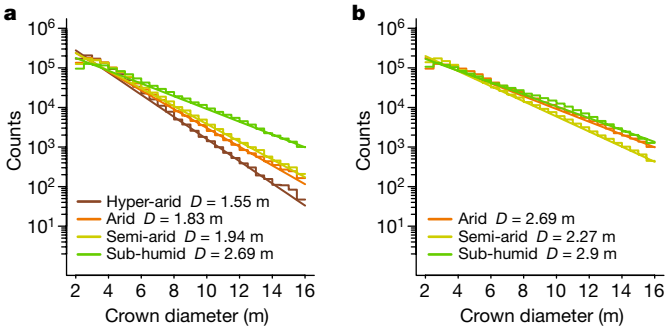

Fig. 4 | Distribution of tree crown sizes. a, **b**, Histograms (bin width = 0.5 m) of crown sizes (range 2–16 m in crown diameter, corresponding to 3–200 m^2 crown size) based on 1 million random samples for each rainfall zone from all trees (**a**) and trees in farmland and urban areas (**b**). The *y* axis has been log-transformed. A model of the form $N(d) = A \times \exp(-d/D)$ was fitted to the tree crown-size distribution for each rainfall zone, in which D is the mean crown diameter (in m) and A is the normalization factor. The lines are the fitted regression lines. There are not enough farmlands in hyper-arid areas for a representative sample size. The pattern agrees well with field-measured trees in arid Senegal (Extended Data Fig. 7b, c).

In a longer-term perspective, knowledge based on individual trees will improve long-term monitoring, environmental assessments and information-driven land-use policies. As such, a database on dryland trees will be an important baseline for policy-makers and stakeholders, as well as initiatives that aim at protecting and restoring trees in arid and semi-arid lands in relation to mitigating degradation, poverty and climate change[12,30].

Online content

Any methods, additional references, Nature Research reporting summaries, source data, extended data, supplementary information, acknowledgements, peer review information; details of author contributions and competing interests; and statements of data and code availability are available at https://doi.org/10.1038/s41586-020-2824-5.

1. Bayala, J., Sanou, J., Teklehaimanot, Z., Kalinganire, A. & Ouédraogo, S. Parklands for buffering climate risk and sustaining agricultural production in the Sahel of West Africa. *Curr. Opin. Environ. Sustain.* **6**, 28–34 (2014).
2. Stringer, L. C. et al. Challenges and opportunities in linking carbon sequestration, livelihoods and ecosystem service provision in drylands. *Environ. Sci. Policy* **19–20**, 121–135 (2012).
3. Schnell, S., Kleinn, C. & Ståhl, G. Monitoring trees outside forests: a review. *Environ. Monit. Assess.* **187**, 600 (2015).
4. LeCun, Y., Bengio, Y. & Hinton, G. Deep learning. *Nature* **521**, 436–444 (2015).
5. Darkoh, M. B. K. The nature, causes and consequences of desertification in the drylands of Africa. *Land Degrad. Dev.* **9**, 1–20 (1998).
6. Ribot, J. C. A history of fear: imagining deforestation in the West African dryland forests. *Glob. Ecol. Biogeogr.* **8**, 291–300 (1999).
7. Fairhead, J. & Leach, M. False forest history, complicit social analysis: rethinking some West African environmental narratives. *World Dev.* **23**, 1023–1035 (1995).
8. Hansen, M. C. et al. High-resolution global maps of 21st-century forest cover change. *Science* **342**, 850–853 (2013).
9. Ickowitz, A., Powell, B., Salim, M. A. & Sunderland, T. C. H. Dietary quality and tree cover in Africa. *Glob. Environ. Change* **24**, 287–294 (2014).
10. Baudron, F., Chavarría, J. Y. D., Remans, R., Yang, K. & Sunderland, T. Indirect contributions of forests to dietary diversity in Southern Ethiopia. *Ecol. Soc.* **22**, 28 (2017).
11. Angelsen, A. et al. Environmental income and rural livelihoods: a global-comparative analysis. *World Dev.* **64**, S12–S28 (2014).
12. Reed, J. et al. Trees for life: the ecosystem service contribution of trees to food production and livelihoods in the tropics. *For. Policy Econ.* **84**, 62–71 (2017).
13. Brito, J. C. et al. Unravelling biodiversity, evolution and threats to conservation in the Sahara-Sahel. *Biol. Rev. Camb. Philos. Soc.* **89**, 215–231 (2014).
14. Brandt, M. et al. Satellite passive microwaves reveal recent climate-induced carbon losses in African drylands. *Nat. Ecol. Evol.* **2**, 827–835 (2018).
15. de Foresta, H. et al. *Towards the Assessment of Trees Outside Forests (Resources Assessment Working Paper 183)* (FAO, 2013).
16. Crowther, T. W. et al. Mapping tree density at a global scale. *Nature* **525**, 201–205 (2015).
17. Axelsson, C. R. & Hanan, N. P. Patterns in woody vegetation structure across African savannas. *Biogeosciences* **14**, 3239–3252 (2017).
18. Schepaschenko, D. et al. Comment on "The extent of forest in dryland biomes". *Science* **358**, eaao0166 (2017).
19. Bastin, J.-F. et al. The extent of forest in dryland biomes. *Science* **356**, 635–638 (2017).
20. Song, X.-P. et al. Global land change from 1982 to 2016. *Nature* **560**, 639–643 (2018).
21. Brandt, M. et al. Reduction of tree cover in West African woodlands and promotion in semi-arid farmlands. *Nat. Geosci.* **11**, 328–333 (2018).
22. Brandt, M. et al. Woody plant cover estimation in drylands from Earth observation based seasonal metrics. *Remote Sens. Environ.* **172**, 28–38 (2016).
23. Reichstein, M. et al. Deep learning and process understanding for data-driven Earth system science. *Nature* **566**, 195–204 (2019).
24. Ronneberger, O., Fischer P. & Brox, T. U-net: convolutional networks for biomedical image segmentation. In *International Conference on Medical Image Computing and Computer-Assisted Intervention* (eds. Navab, N. et al.) 234–241, (Springer, 2015).
25. Muller-Landau, H. C. et al. Comparing tropical forest tree size distributions with the predictions of metabolic ecology and equilibrium models. *Ecol. Lett.* **9**, 589–602 (2006).
26. Buchhorn, M. et al. Copernicus global land service: land cover 100 m: epoch 2018: Africa demo. https://land.copernicus.eu/global/products/lc (2019).
27. Wood, S. A. & Baudron, F. Soil organic matter underlies crop nutritional quality and productivity in smallholder agriculture. *Agric. Ecosyst. Environ.* **266**, 100–108 (2018).
28. Sandbrook, C., Sunderland, T., & Tu, T. N. in *Forests and Food* (eds Bhaskar, V. et al.) 73–136 (Open Book, 2015).
29. Rasolofoson, R. A., Hanauer, M. M., Pappinen, A., Fisher, B. & Ricketts, T. H. Impacts of forests on children's diet in rural areas across 27 developing countries. *Sci. Adv.* **4**, eaat2853 (2018).
30. Griscom, B. W. et al. Natural climate solutions. *Proc. Natl Acad. Sci. USA* **114**, 11645–11650 (2017).

Methods

No statistical methods were used to predetermine sample size. The experiments were not randomized and investigators were not blinded to allocation during experiments and outcome assessment.

Overview

This study establishes a framework for the detection of tree crowns in satellite imagery of very high spatial resolution. We used a supervised deep-learning approach to detect single woody plants in panchromatic and pansharpened NDVI[31] images at 0.5-m spatial resolution. Owing to the scattered nature of savannah trees, their crowns stand out as objects with a high NDVI value—in contrast to their surroundings, which have low NDVI values in the dry season. Visually, it is thus straightforward to identify tree crowns in the satellite images, and we manually delineated and annotated 89,899 individual trees along a north–south gradient, capturing the full range of landscape variation. The manually mapped crowns were used to train the deep-learning model, which was subsequently used to predict crowns for the entire study area. The resulting spatial database includes each detected tree, its crown size in m^2, and mean annual rainfall, land use and soil.

Additionally, we derived several raster maps consisting of 100 × 100-m (1-ha) grids from the database, considering the centroids of all identified tree crowns >3 m^2 (Extended Data Figs. 5, 6): the mean crown size per hectare (the mean size of all crowns within this grid), the total canopy cover per hectare (the area of the grid covered by mapped crowns in per cent), the density of crowns per hectare, the density of shrubs (3–15 m^2), the density of small trees (15–50 m^2), the density of large trees (50–200 m^2) and objects exceeding 200 m^2, which are either very large trees or clumped trees that could not be separated. By fitting an exponential model over the crown size distribution, we estimate the percentage of trees with a crown <3 m^2.

When training the deep-learning model, we only included training objects that showed a clear crown area and shadow, which excludes small bushes and grass tussocks from our classification. The uncertainty of trees with a crown size <3 m^2 is relatively high, because shrubs of this size are dynamic: they grow quickly but are often removed by land clearing or fire. This can lead to differences in mosaics that are composites of images from different dates. Additional uncertainty is caused by small trees being located beneath larger trees.

Satellite imagery

We assembled more than 50,000 DigitalGlobe multispectral images from the QuickBird-2, GeoEye-1, WorldView-2 and WorldView-3 satellites, collected from 2005–2018 (in November to March) from 12° to 24° N latitude within Universal Transverse Mercator zones 28 and 29. These images were obtained through the NextView licence from the National Geospatial Intelligence. The images used were not atmospherically corrected, were not adjusted for off-nadir viewing and were not intercalibrated among the four DigitalGlobe satellites (Extended Data Fig. 8).

All multispectral and panchromatic bands associated with the images were orthorectified to a common mapping basis. We next pansharpened all multispectral bands to the 0.5-m scale with the associated panchromatic band. The locational uncertainty of pixels at the 0.5-m scale from orbit is approximately ±11 m, considering the root mean square location errors among the QuickBird, GeoEye-1, WorldView-2 and WorldView-3 satellites (Supplementary Table 1).

We formed the NDVI from every image in the traditional way[31], from the pansharpened red and near-infrared bands. We also associated the panchromatic band with the NDVI band and ensured the panchromatic and NDVI bands were highly coregistered. The NDVI was used to distinguish tree crowns from non-vegetated background, because the images were taken from a period during which only woody plants are photosynthetically active in this area[22].

A set of decision rules was applied to select images for the mosaic, consisting of 25 × 25-km tiles. We used imagery collected between November and March, because November is the start of the dry season. The first round of scoring considered percentage cloud cover, sun elevation angle and sensor off-nadir angle: preference is given to imagery that has lower cloud cover percentage, then higher sun elevation angle, and finally view angles closest to nadir. In the second round of scoring, selections were prioritized to favour date and off-nadir view angles: preference was given first to imagery from November to January, with off-nadir angle <15° degrees; preference was next given to imagery from November to January, with off-nadir angle between 15° and 30° degrees; preference was next given to imagery from February or March, with off-nadir angle less than 15° degrees; and finally to imagery from February or March, with off-nadir angle between 15° and 30° degrees. Image mosaics are necessary to eliminate the multiple counting of trees. This resulted in 11,128 images that were used for the study. Overall, 3% of the study area has been masked owing to insufficient data quality. Because most of these areas are located in the desert with a very low tree cover, we do not expect any effect on the statistics presented.

Mapping tree crowns with deep learning

We used state-of-the-art methods from the field of deep learning[4,23] to automatically segment the tree crowns—that is, to detect tree crowns in the input images. The segmented areas were then converted to polygons for counting the trees and measuring their crown size.

Deep learning has been the main driver of progress in artificial intelligence over the past decade. It emerged from research in artificial neural networks and refers to building models organized in layers of computational units, which develop more and more abstract representations of the underlying input data. Deep learning has proven to be a disruptive technology in many areas (speech and natural language processing, medical image analysis and so on), and we expect a similar impact in remote sensing. The advantages and the great potential of using deep learning in Earth system science have previously been summarized[23].

Deep learning for image analysis is almost synonymous with applying convolutional neural networks[4,23,32]. These networks have layers that essentially perform convolutions, in which convolutional filters move over the spatially structured input to produce spatially structured outputs known as feature maps. Convolution is a fundamental operation in signal processing. The parameters of the convolutional filters define the features that are extracted. However, instead of using predefined convolutional filters (for example, designed to detect edges, ridges or blobs), the parameters of the filters in a convolutional neural network are learned similarly to weights in a standard neural network. When used for classification or regression, the output of the final convolutional layer typically serves as the input to a standard neural network. This is not the case for fully convolutional neural networks[24,33,34], which mark the state of the art in semantic image segmentation; ref. [35] and ref. [36] provide for examples in street scene and medical image segmentation, respectively. Fully convolutional neural networks for 2D image segmentation map a 2D image or image patch to a segmentation map (typically of the same spatial dimensionality as the input), and assign a class to each input pixel.

We used the U-Net architecture as previously proposed[24], slightly modified as previously described[37,38]. In medical image segmentation, the U-Net architecture has proven to work robustly over a variety of tasks[36,37], and we adopted this approach for tree crown segmentation. The input was downsampled after each of the first half of the convolutional layers, and then upsampled before each of the second half of the convolutional layers. In the upsampling path, the inputs to the convolutions were combined with the outputs of the corresponding sizes from the downsampling path. This architecture allowed the simultaneous processing of an input image at different spatial scales.

We did not use dropout[39], but added batch normalization after each convolution block[40]. Furthermore, we used nearest-neighbour

upsampling followed by convolution in the standard upsampling path[41]. Further, the loss function used during training (that is, the objective function that penalizes the discrepancy between the true labels and the predictions made by the model) was the Tversky loss[42], which deals better with class imbalance in segmentation compared to the common classification loss. We used α and β values of 0.5.

The fully convolutional neural network received the NDVI and the panchromatic band as inputs (both 0.5 × 0.5-m spatial resolution). We generated data patches from 494 rectangles (in total 75 km^2) distributed from north to south and representing the full range of different landscapes (Extended Data Fig. 4), also including image boundaries, burned areas and areas affected by dust and cloud cover. A special focus was set to cover different dates, so that the algorithm could capture both trees with few or no leaves, and trees in full leaf. We marked the crown areas of 89,899 trees of all sizes as polygons within these rectangles, which were converted to rasterized images (tree or no-tree segmentation maps). Typically, two conditions had to be fulfilled for a crown to be marked during the manual labelling process: (a) the NDVI value had to be clearly higher than the surrounding (only trees have green leaves in the dry season), and (b) a shadow had to be seen. These conditions allowed us to distinguish tree crowns from grass tussocks, bushes and rocks. Exceptions were dry-season deciduous trees (for example, *Adansonia digitata*) that were large enough to form a visible crown without leaves, a situation that was included in the training data. The selection of training areas followed the principle of selecting the most challenging and extreme situations.

The disaggregation of clumped trees was achieved by highlighting spaces between different crowns during the learning process. Inspired by a previously proposed strategy[24] for separating touching cells in microscopy imagery, we provided pixel-wise weight maps during training, in which pixels corresponding to canopy gaps were given a larger weight (10 if a pixel corresponded to a gap pixel, and 1 otherwise). The weight maps can be easily derived from the distances between canopy polygons (Extended Data Fig. 3). Incorporating the weights into the overall loss function forced the network to learn the gaps, and the resulting model tended to avoid making false predictions at canopy gaps, which also led to the predicted canopies slightly shrinking in size in areas of dense tree cover.

Owing to the high latitudinal variations in vegetation and soil background and to avoid misclassifications in the very sparsely vegetated Sahara desert, we trained two separate models. Firstly, we trained a model for the low-rainfall desert region ranging from 24° N to about 17° N latitude and ending at the Senegal River, which we refer to as the Sahara model. For training the second model, data from the entire study area were used, but only applied for the Sahel and Sudan area, which we thus refer to as the Sahel and Sudan model. Out of 494 rectangles, 188 rectangles were used for the Sahara model and all 494 rectangles were used to train the Sahel and Sudan model. Rectangles located in the Sahel and Sudan area included a much higher number of trees.

Next, we randomly sampled patches with a size of 256 × 256 pixels (each pixel corresponds to 0.5 × 0.5 m) from the rectangles. We locally normalized the patches with a 40% probability (both the NDVI and panchromatic band) to zero mean and unit s.d., and the remaining 60% were normalized with mean and s.d. of the rectangle (that is, of the bigger area from which the patch was extracted). The probability of the local normalization affects the detection and misclassification, which need to be finely balanced.

Data augmentation is a technique to improve the generalization performance of convolutional neural networks. The training data were extended by generating additional artificial and transformed training images. We used several transformations: cropping and zooming; piecewise affine, perspective transformation; and linear contrast enhancement. The training data were used for the gradient-based optimization of the U-Net parameters and the training progress was monitored by computing the validation and loss error. The parameters with the lowest error defined the final model. Selection of appropriate hyper-parameters, normalization probability and augmentations was based on the training dataset and visual inspection of randomly chosen and independent areas. The challenge was to keep the balance between detecting trees that were hardly visible (for example, those without leaves) on the one hand, and separating touching canopies and avoiding misclassifications on the other hand.

The prediction was then done for 256 × 256-pixel patches with a 12% overlap of the patches (a technique sometimes referred to as test time augmentation). If a woody canopy was predicted by one of the predictions in the overlapping area, the pixel was classified as canopy area. Each patch was normalized before the prediction, which helped to cope with varying atmospheric settings and reflectance in the satellite imagery and improved the model prediction in areas with cloud cover or burned surface.

Before moving on to the evaluation based on independent test and field data, we studied the effect of image quality on prediction performance by comparing the predicted crowns >3 m^2 with the manually labelled 89,899 trees within the 494 rectangles (Extended Data Table 1), grouped according to different image properties. The regression slope indicates that tree cover and density in later-dry season images (mainly March) are underestimated by up to one fourth, and also that for images with a low sun azimuth angle and large off-nadir angle, tree cover tends to be underestimated. As the availability of suitable images in the early dry season is limited (13% of the area is covered by images from February and March), this has to be kept in mind when interpreting the numbers reported (Extended Data Fig. 8).

Evaluation

To evaluate the generalization performance of our model, we created a test dataset by randomly distributing 100 plots (not overlapping with the training data), each with a size of 256 × 256 pixels, over the study area. The test dataset was created independently and was not included in the model development and parameter selection process, avoiding the bias of adaptive data analysis. We manually labelled all tree crowns in the test plots. Overall, 5% of the labelled trees were missed in the final prediction, most having a size <15 m^2 (Extended Data Table 2). Moreover, 25% of the area covered by labelled trees was missed in the predictions, with trees below 50 m^2 contributing most to the missed canopy areas (75% true-positive rate), whereas 2% of the area labelled as background was classified as tree canopy (false-positive rate). In total, 3.8% of the labelled trees were not predicted as individual trees but were included in clumped canopies.

We further conducted a per-plot comparison between the labelled and the predicted tree crowns. The correlation was very high with r^2 values of 0.97 (slope = 1.00) for tree density, 0.95 (slope = 0.87) for canopy cover and 0.92 (slope = 0.77) for mean crown size (Extended Data Fig. 2, Extended Data Table 2). The slight underestimation of the canopy cover and mean crown size (expressed by slope values below 1) for areas of high canopy cover is a result of the hyper-parameter selection and disaggregation of clumped canopies (Extended Data Fig. 2).

After having gained confidence in our model through the evaluation using the test data, we compared the predictions with data from two field campaigns in Senegal, one conducted in the arid (September 2016) and one in the semi-arid (January 2018) zone: Extended Data Fig. 4 shows the location of the sites. We obtained the crown size of 102 trees >3 m^2 by measuring the longest spread and the longest cross-spread of the canopy. The crown size of each field-measured tree was compared with the deep-learning prediction, achieving a very high accuracy (r^2 = 0.89, mean absolute error = 8 m^2)—but often showing smaller crown sizes in the satellite-data-derived trees (slope = 0.71). This difference may be caused by the different perception of the crown, which is assumed to be an ellipse covering the outermost extent in the field data, whereas the satellite-based method followed the crown shape

more precisely. The difference is systematic over different satellite images and field campaigns.

We also used field data from a campaign in arid Senegal in September 2015. As previously described[21], all trees in 144 squared plots of 0.25 ha each were surveyed. Owing to a shift in the satellite data and missing GPS coordinates of the field-measured trees, we could not use these data for a direct per-plot comparison with the predicted tree crowns, but only for a comparison of the overall density and size distribution. The 974 field measured trees >3 m^2 had a density of 28.4 trees per hectare, which corresponds well with the predicted trees of the area (27.2 trees per hectare), and also the crown diameter distribution confirms our results shown in Fig. 4 and Extended Data Fig. 7b, c.

Environmental data

We used the 'Climate Hazards Group Infrared Precipitation with Station' (CHIRPS) rainfall data to estimate annual rainfall in 5.6-km grids[43]. We averaged the available data from 1982 to 2017 and extracted the mean annual rainfall for each mapped tree and interpolated it to 100 × 100-m resolution (bilinear). Mean CHIRPS data were also used to classify the study area into hyper-arid (0–150 mm yr^{-1} mean annual rainfall), arid (150–300 mm yr^{-1}), semi-arid (300–600 mm yr^{-1}) and sub-humid (600–1,000 mm yr^{-1}) zones.

Copernicus land-use data were included to determine human-managed areas from the 'urban' and 'cropland' classes[26] (Extended Data Fig. 4). The savannah classes were grassland, shrubland, open forest and bare areas. These data are available at a 100-m resolution for 2016. Soil maps were derived from a previous publication[44].

Software

Only free and open-source software was used for data analysis: RStudio (1.2), GRASS GIS (7.8), QGIS (3.10) and GDAL tools (3.0). The deep-learning code was written in Python (3.7) using tensorflow (2.0).

Reporting summary

Further information on research design is available in the Nature Research Reporting Summary linked to this paper.

Data availability

Global tree cover maps are available at http://earthenginepartners.appspot.com/science-2013-global-forest. CHIRPS rainfall data are freely available at the Climate Hazard Group (https://www.chc.ucsb.edu/data/chirps). The Copernicus land-use map can be downloaded at https://land.copernicus.eu/global/. Commercial very-high-resolution satellite images were acquired by NASA, under a NextView Imagery End User Licence Agreement. The copyright remains with DigitalGlobe, and redistribution is not possible. However, the derived products produced in this Article are made publicly available at the Oak Ridge National Laboratory at https://doi.org/10.3334/ORNLDAAC/1832. Any further relevant data are available from the corresponding authors upon reasonable request.

Code availability

The tree detection framework based on U-Net is publicly available at https://doi.org/10.5281/zenodo.3978185; support and more information are available from A.K. (kariryaa@uni-bremen.de or ankit.ky@gmail.com).

31. Tucker, C. J. Red and photographic infrared linear combinations for monitoring vegetation. *Remote Sens. Environ.* **8**, 127–150 (1979).
32. LeCun, Y. et al. Handwritten digit recognition with a back-propagation network. In *Advances in Neural Information Processing Systems 2* (ed. Touretzky, D. S.) 396–404 (Neural Information Processing Systems Foundation, 1990).
33. Long, J., Shelhamer, E. & Darrell, T. Fully convolutional networks for semantic segmentation. In *Proc. IEEE Conference on Computer Vision and Pattern Recognition (CVPR)* (eds Bischof, H. et al.) 3431–3440 (IEEE Computer Society, 2015).
34. Sermanet, P. et al. OverFeat: integrated recognition, localization and detection using convolutional networks. Preprint at https://arxiv.org/abs/1312.6229 (2014).
35. Cordts, M. et al. The cityscapes dataset for semantic urban scene understanding. In *Proc. IEEE Conference on Computer Vision and Pattern Recognition (CVPR)* (eds Bajcsy, R. et al.) 3213–3223 (IEEE Computer Society, 2016).
36. Simpson, A. L. et al. A large annotated medical image dataset for the development and evaluation of segmentation algorithms. Preprint at https://arxiv.org/abs/1902.09063 (2019).
37. Perslev, M., Dam, E., Pai, A. & Igel, C. One network to segment them all: a general, lightweight system for accurate 3D medical image segmentation. In *Medical Image Computing and Computer Assisted Intervention (MICCAI)* (eds Shen, D. et al.) 30–38 (Springer, 2019).
38. Koch, T., Perslev, M., Igel, C. & Brandt, S. Accurate segmentation of dental panoramic radiographs with U-nets. In *Proc. IEEE International Symposium on Biomedical Imaging (ISBI)* (eds Davis, L. et al.) 15–19 (IEEE Computer Society, 2019).
39. Srivastava, N. et al. Dropout: a simple way to prevent neural networks from overfitting. *J. Mach. Learn. Res.* **15**, 1929–1958 (2014).
40. Ioffe, S. & Szegedy, C. Batch normalization: accelerating deep network training by reducing internal covariate shift. In *International Conference on Machine Learning (ICML)* (eds Bach, F. & Blei, D.) 448–456 (PMLR, 2015).
41. Odena, A., Dumoulin, V. & Olah, C. Deconvolution and checkerboard artifacts. *Distill* https://distill.pub/2016/deconv-checkerboard/ (2016).
42. Sadegh, S., Salehi, M., Erdogmus, D. & Gholipour, A. Tversky loss function for image segmentation using 3D fully convolutional deep networks. In *International Workshop on Machine Learning in Medical Imaging* (eds Wang, Q. et al.) 379–387 (Springer, 2017).
43. Funk, C. et al. The climate hazards infrared precipitation with stations—a new environmental record for monitoring extremes. *Sci. Data* **2**, 150066 (2015).
44. Hengl, T. et al. Mapping soil properties of Africa at 250 m resolution: random forests significantly improve current predictions. *PLoS ONE* **10**, e0125814 (2015).

Acknowledgements We thank Maxar for providing commercial satellite data through the NextView Imagery End User Licence Agreement of the National Geospatial Intelligence Agency. This research is part of the Blue Waters sustained peta-scale computing project, which is supported by the National Science Foundation (awards OCI-0725070 and ACI-1238993), the State of Illinois and—as of December 2019—the National Geospatial-Intelligence Agency. Blue Waters is a joint effort of the University of Illinois at Urbana-Champaign and its National Center for Supercomputing Applications. M.B. was financed by an AXA post-doctoral research grant and a DFF Sapere Aude grant (9064-00049B). A.K. and J. Schöning were funded by a Lichtenberg Professorship of the Volkswagen Foundation. J.C. acknowledges ANR grants (CEBA, ref. ANR-10-LABX-25-01 and TULIP: ANR-10-LABX-0041). We acknowledge support by the Villum Foundation through the project 'Deep Learning and Remote Sensing for Unlocking Global Ecosystem Resource Dynamics' (DeReEco). L.V.R. was funded by the European Research Council (ERC) under the European Union's Horizon 2020 research and innovation programme (grant agreement no. 853222 FORESTDIET). This Article contributes to the Global Land Programme, glp.earth. We thank the group around M. Hansen for making their product on global tree cover freely available; T. Lee for suggesting this project; K. Murphy for his support; D. Duffy for his high-performance computing support; S. Keesey, C. Williamson, C. Crittenden, K. Allen, M. Schlenk, B. Bates and K. Peterman for their satellite data contributions; and W. Kramer and B. Bode for their high-performance computing support. Approved for public release, no. 20-732.

Author contributions M.B., C.J.T., R.F. and K.R. designed the study. C.J.T., J. Small, S.S., J.M., E.R., E.G. and K.M. prepared and processed the satellite data. M.B. selected the training data. A.K. wrote the code for the deep-learning framework, supported by S.L., J. Schöning, F.G., J.M. and C.I. M.B., C.A., A.K. and J.C. conducted the analyses. Interpretations were done by P.H., J.C., R.F., K.R., L.K., O.M., A.M. and A.A.D. M.D, C.A. and R.F. collected the field data. K.R., M.B. and L.V.R. wrote the first manuscript draft with contributions by all authors. M.B. designed the figures.

Competing interests The authors declare no competing interests.

Additional information

Supplementary information is available for this paper at https://doi.org/10.1038/s41586-020-2824-5.

Correspondence and requests for materials should be addressed to M.B. or C.J.T.

Peer review information *Nature* thanks Niall Hanan, Liming Zhou and the other, anonymous, reviewer(s) for their contribution to the peer review of this work.

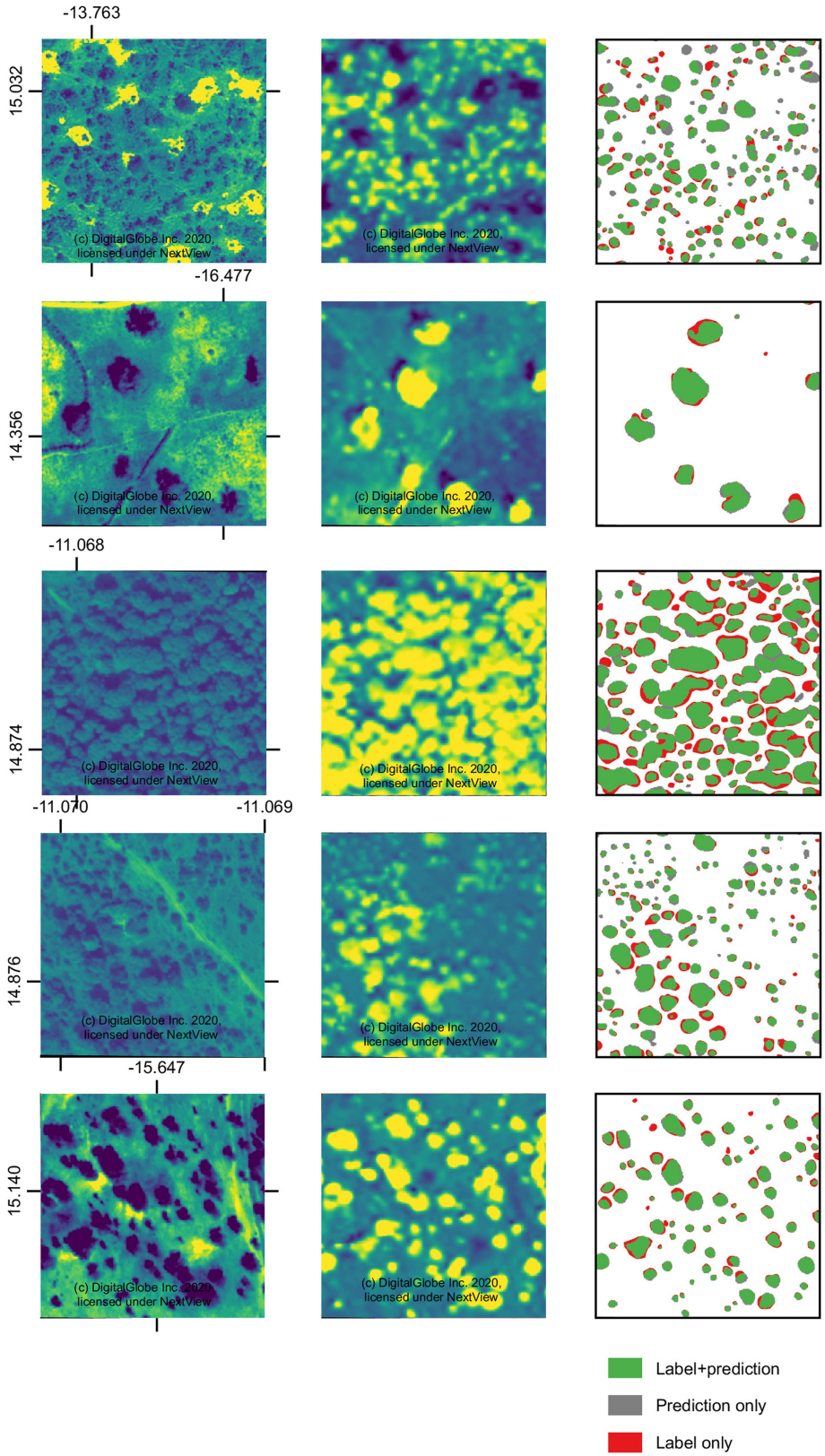

Extended Data Fig. 1 | Predicting tree crowns. This set of 256 × 256-pixel plots from the independent test dataset shows the capabilities of the convolutional neural network model to predict trees (right column) from panchromatic images (left column) and NDVI (central column) at 0.5-m resolution.

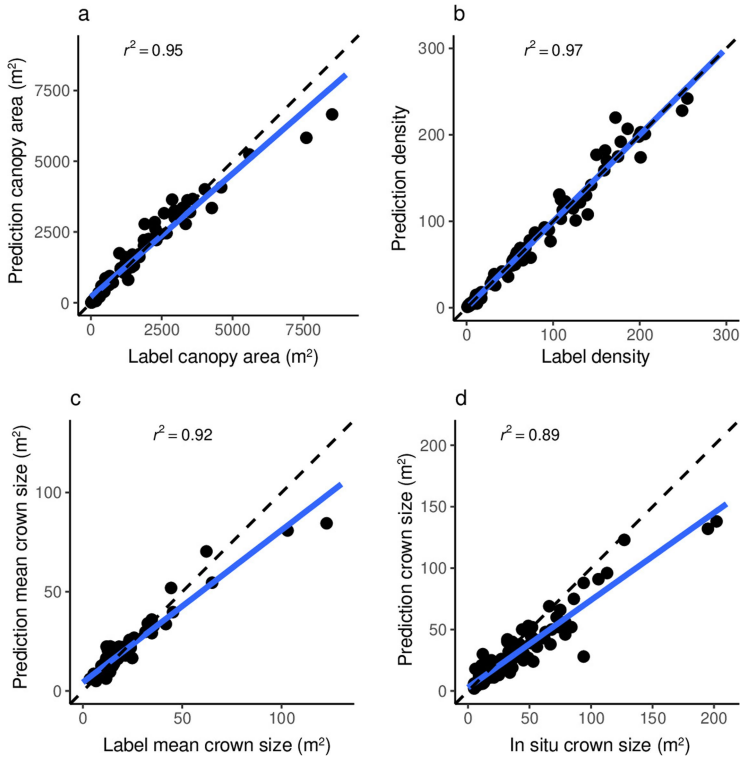

Extended Data Fig. 2 | Evaluation. a, Manually labelled tree crowns from the independent test dataset are compared against predictions. The comparison is done for 100 random plots each having 256 × 256 pixels. Here, the canopy area (in m^2) of the trees in the plots is compared. **b**, As in **a**, but for the density (the number of labelled or predicted trees per plot). **c**, As in **a**, but for mean crown size per plot. **d**, The crown sizes of 102 in situ measured trees from 2 field campaigns in Senegal (Extended Data Fig. 4) are compared with the predicted ones. Extended Data Table 2 provides more details. $n = 100$ plots with 256 × 256-pixel size.

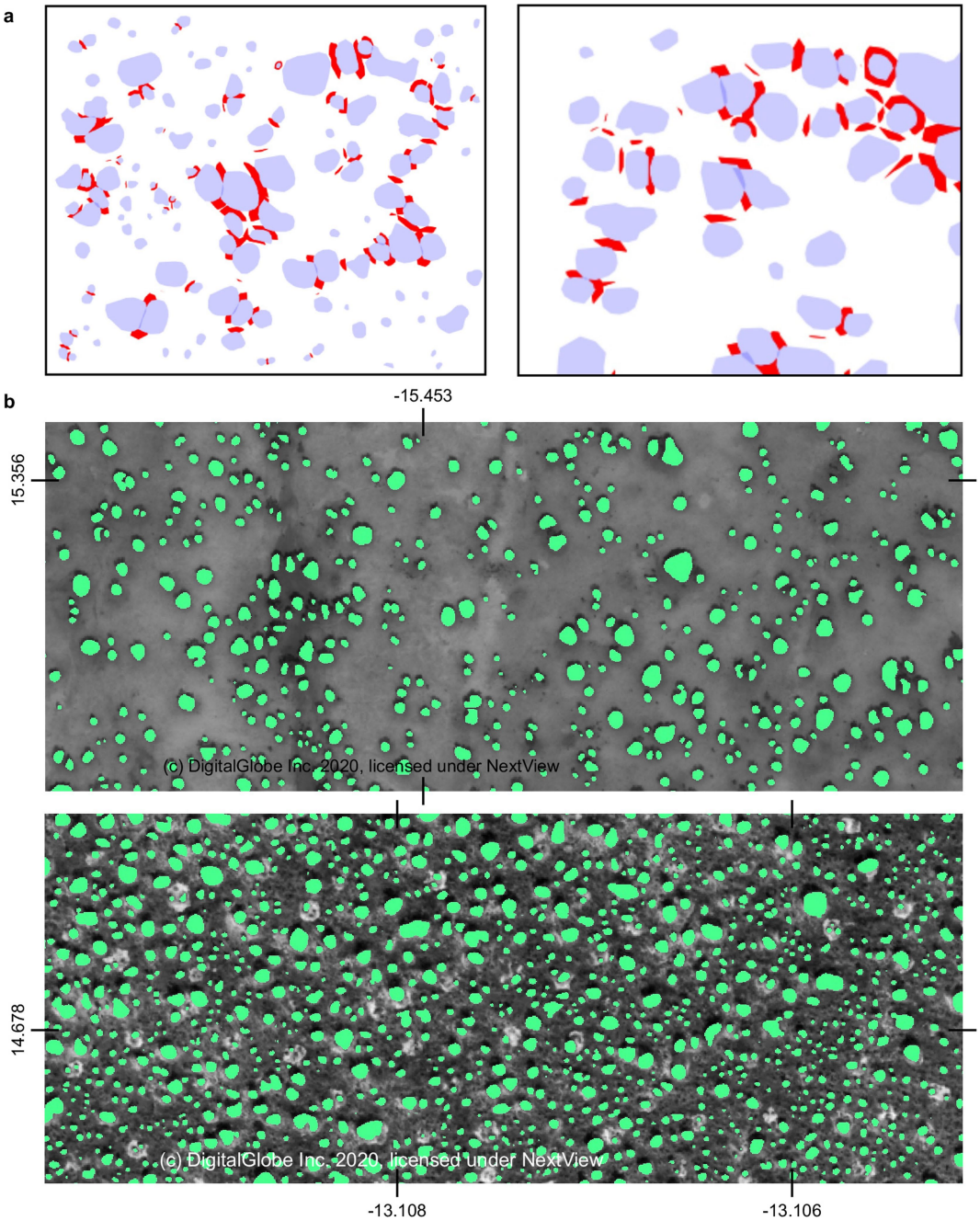

Extended Data Fig. 3 | Mapping individual tree crowns. a, Before training the model, the spaces between labelled tree crowns (light blue) were filled (red) and given a higher weight. During training, the model was penalized more strongly for wrongly classifying gap pixels compared to other misclassifications. As a result, tree crowns that touch or are close to each other could be reliably separated. **b**, Examples of predicted trees (green), showing that most trees standing close to each other were mapped as individuals trees.

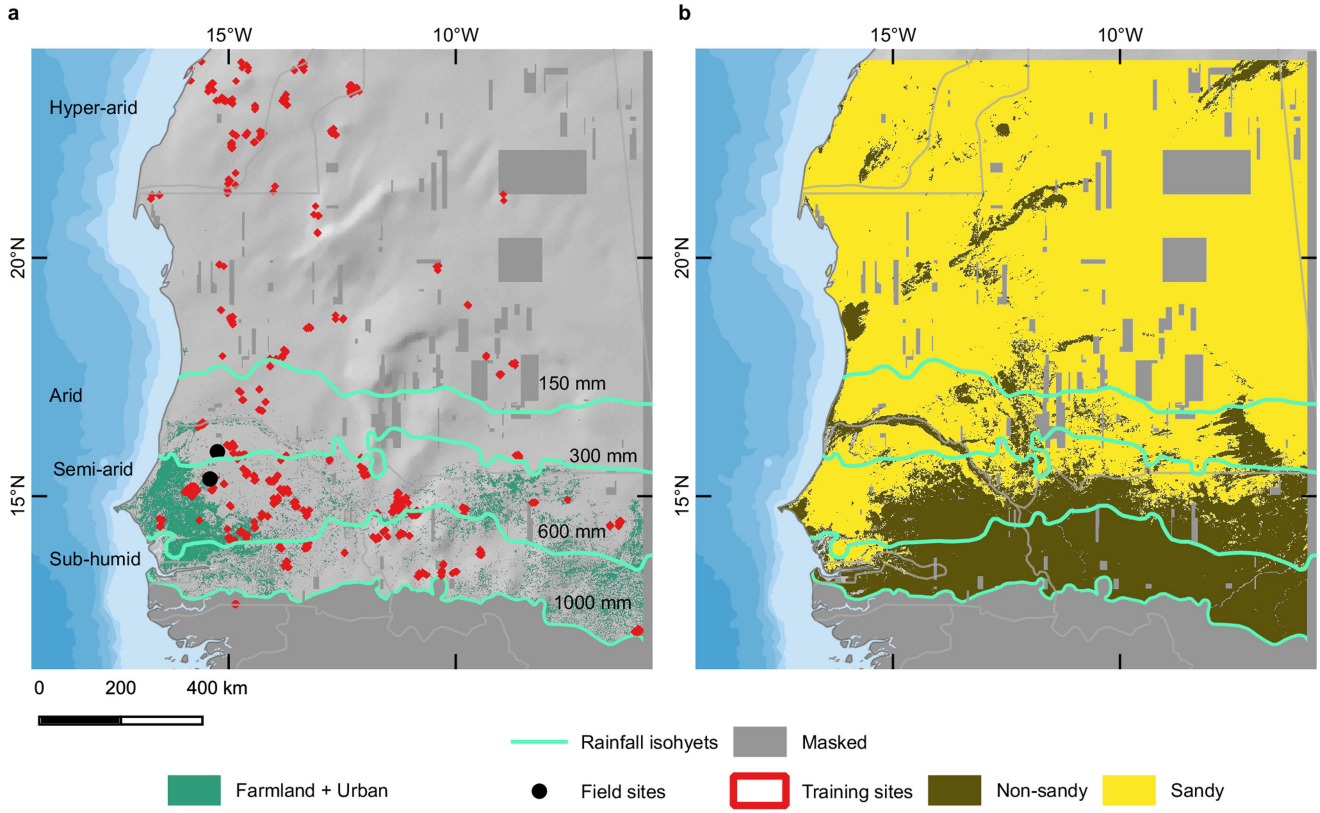

Extended Data Fig. 4 | Overview of training sites and study area. The study area for the wall-to-wall mapping is the westernmost part of the Sahara and Sahel. It represents a typical north–south ecological and climatic gradient, starting in the Sahara Desert in hyper-arid areas (rainfall of 0–150 mm yr^{-1}) with a sparse vegetation coverage, over arid (rainfall of 150–300 mm yr^{-1}) and semi-arid (rainfall of 300–600 mm yr^{-1}) Sahelian rangelands and croplands, up to sub-humid (rainfall of 600–1,000 mm yr^{-1}) Sudanian lands, where shrublands turn into forests. **a**, The locations of the manually drawn 89,899 tree crowns used for training the model are shown in red. CHIRPS rainfall[43] was used to delineate the rainfall zones. The land use for farmland and urban is from Copernicus Global Land[26]. In situ data were collected at the field sites around Widou and Dahra in Senegal. Areas of insufficient data quality and beyond rainfall of 1,000 mm yr^{-1} were masked. **b**, The region was analysed for sandy (>70% sand content) and non-sandy areas[44].

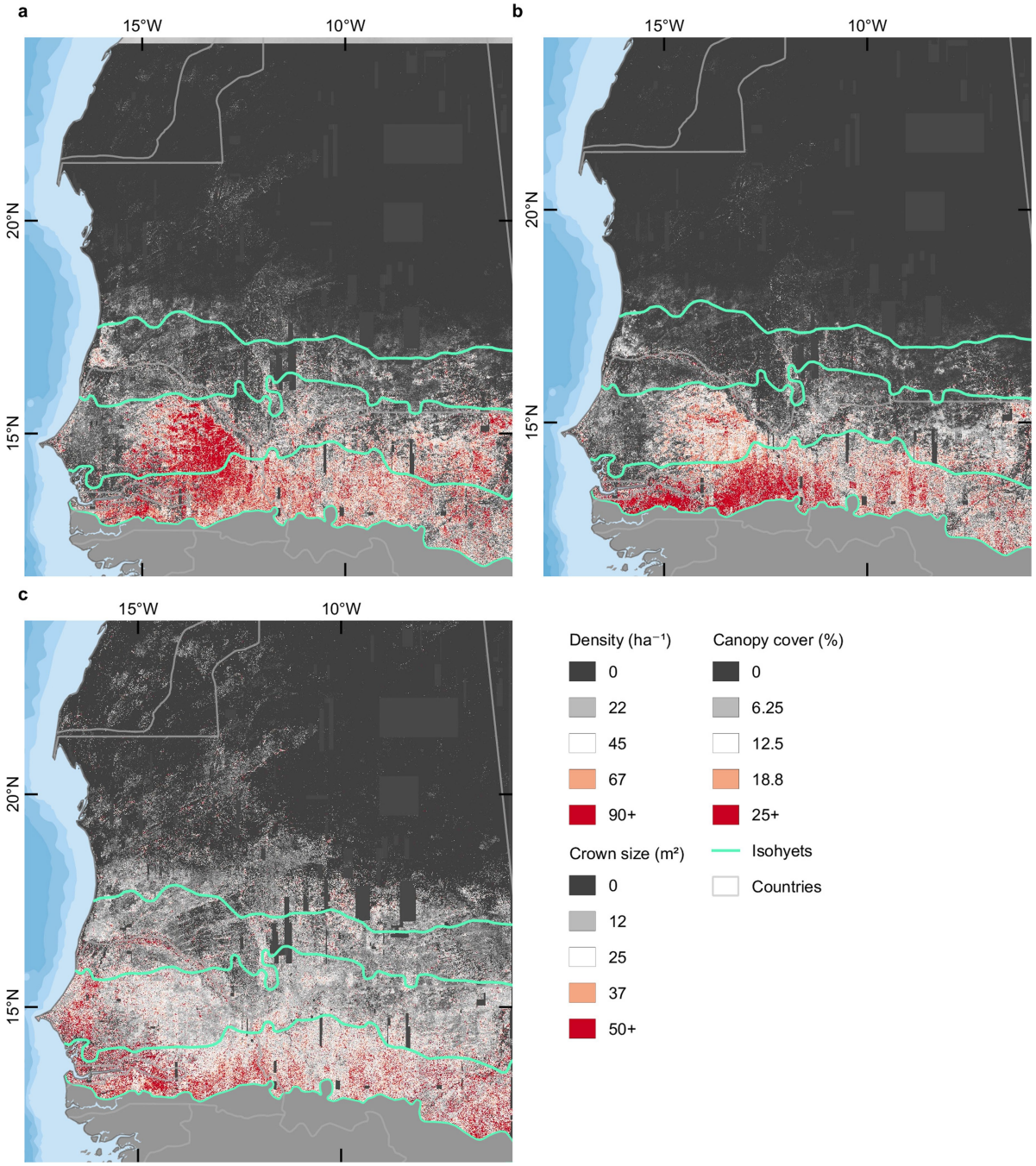

Extended Data Fig. 5 | Variables mapped in this study. a, The density of trees with a crown size larger 3 m^2 per hectare. **b**, The canopy cover. **c**, Mean crown size. All variables were mapped by 100 × 100-m (1-ha) grids. Rainfall isohyets of 150, 300, 600 and 1,000 mm yr^{-1} are also shown.

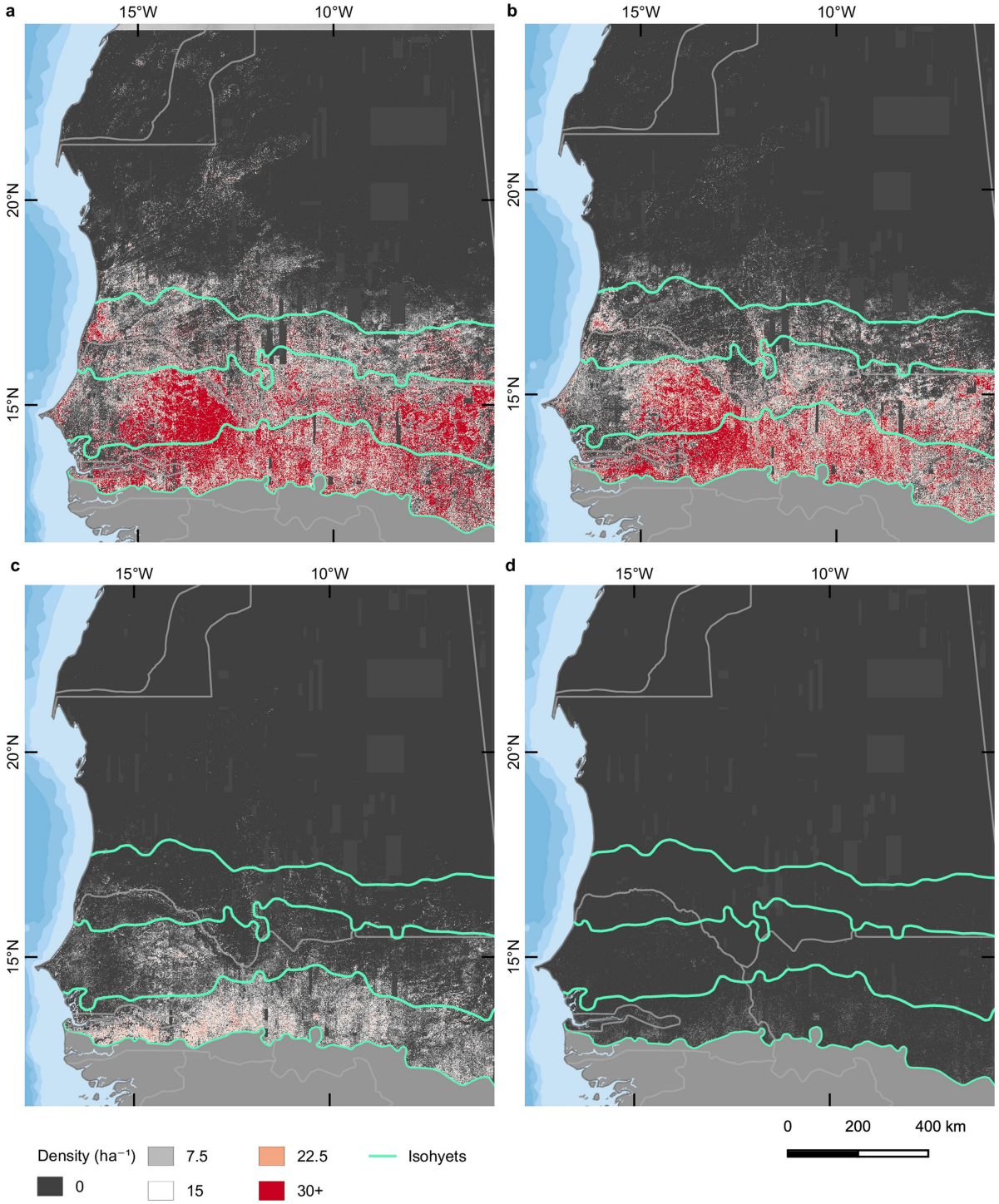

Extended Data Fig. 6 | Tree density classes. a–d, The tree density per hectare is shown for different crown size classes: 3–15 m^2 (**a**), 15–50 m^2 (**b**), 50–200 m^2 (**c**), and >200 m^2 (**d**). Trees in the class >200 m^2 typically do not represent individual tree crowns, but instead reflect closed-canopy areas. Trees <3 m^2 are not shown, owing high uncertainty in this class.

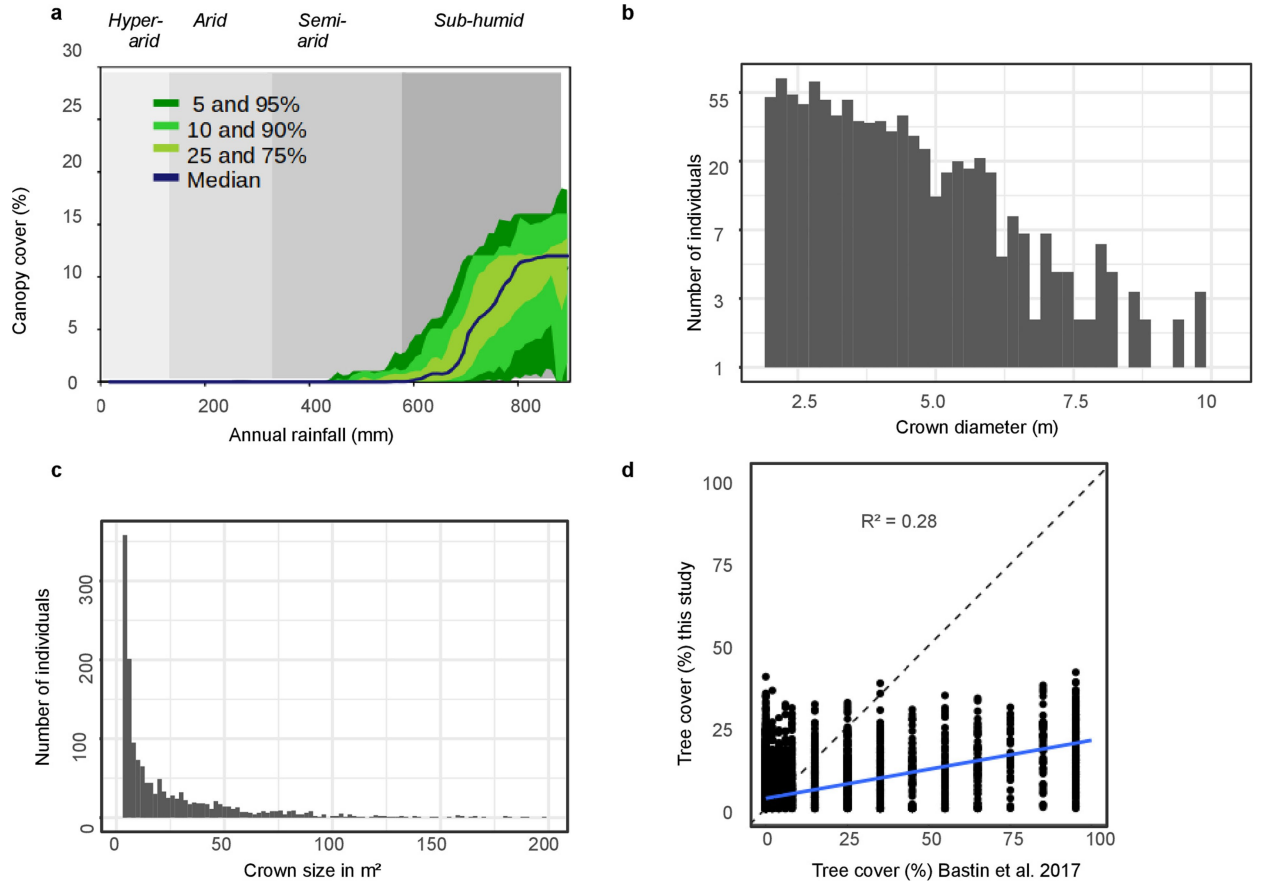

Extended Data Fig. 7 | Comparisons with other datasets. a, Canopy cover of the study area from ref. [8]. **b**, Field-measured crown diameter (derived from crown size 3–200 m^2) of 811 individual trees measured in situ in the Ferlo of Senegal[21]. The *y*-axis has been log-transformed. **c**, As in **b**, but for the crown size and without log transformation. **d**, Woody cover derived from individual trees differs from the current state-of-the-art tree cover map from ref. [19]. $n = 4{,}017$ grids; $r^2 = 0.28$.

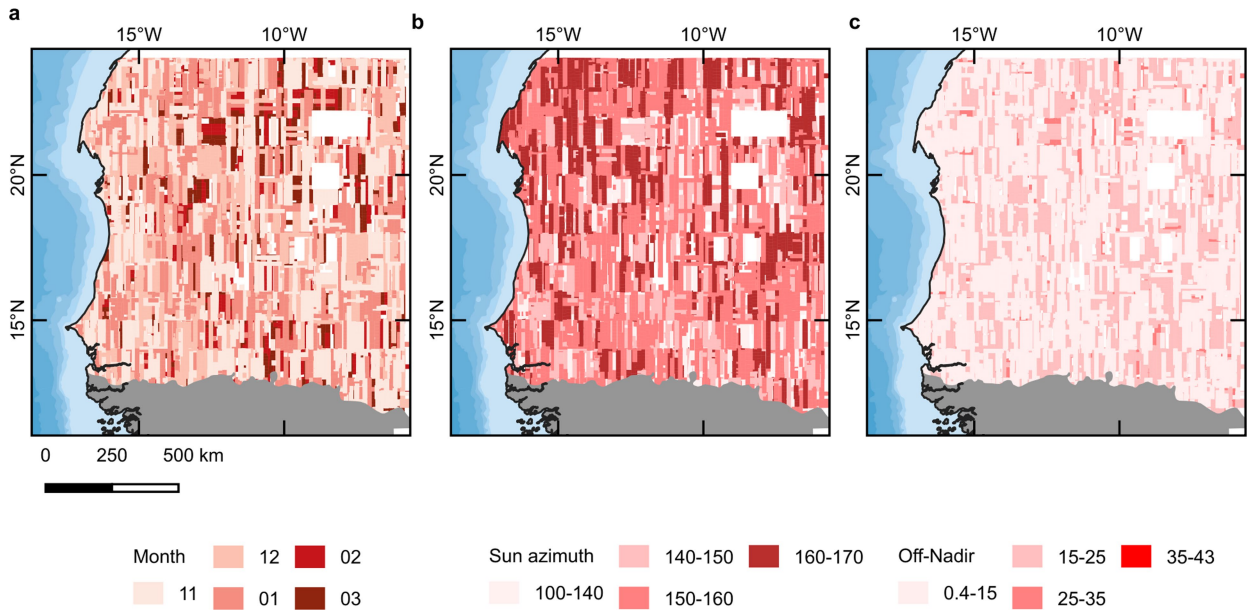

Extended Data Fig. 8 | Overview of satellite images. We used 11,128 multispectral images from the QuickBird-2, GeoEye-1, WorldView-2 and WorldView-3 satellites, acquired from November to March of 2005–2018. Priority was set to images from the early dry season (starting in November), and an off-nadir angle of <25°. Although the model has been trained and validated to work for late-dry season images, the uncertainty is higher in February and March. **a**, Image acquisition months. **b**, Sun azimuth at the image acquisition time. **c**, Off-nadir angle shown for each image.

Extended Data Table 1 | Performance in relation to image quality

	Plots	Density (r^2)	Density (slope)	Canopy (r^2)	Canopy (slope)
ALL	432	0.96	0.97	0.97	0.96
November	111	0.96	0.99	0.97	0.98
December	91	0.95	0.98	0.95	0.92
January	161	0.96	0.93	0.96	0.93
February	34	0.97	0.92	0.98	0.98
March	35	0.95	0.85	0.95	0.76
Off Nadir < 15	313	0.95	0.97	0.97	1.03
Off Nadir >= 15	119	0.97	0.96	0.97	0.87
Sun Azimuth 100-140	58	0.95	0.9	0.99	0.82
Sun Azimuth 140-150	122	0.93	0.95	0.98	1.04
Sun Azimuth 150-160	204	0.96	0.96	0.95	0.95
Sun Azimuth 160-180	83	0.99	1.03	0.97	1

To study the effect of image quality on the model, manually labelled tree crowns (n = 89,899) from our training dataset are compared against predictions. The comparison is done for 432 plots of varying sizes (plots without trees have been removed). Here the density (the number of trees per plot) and the canopy area (in m^2) is compared between the plots. Extended Data Figure 8 shows the spatial distribution of the classes. The slope can be used as a measure of under- or over-estimation. A slope of 1 is a perfect fit; values below 1 indicate underestimation in the prediction. We conclude that satellite data from November and December with off-nadir view angles <15° are preferable.

Extended Data Table 2 | Evaluation

	Number	Missed	Missed (%)	Area (m²)	Missed area (m²)	Missed area (%)	Missed % from total area
ALL	5,697	301	5	116,600	29,458	25	25
<3 m²	405	18	4	468	233	50	0
3-15 m²	3,308	218	7	27,225	9,708	36	8
15-50 m²	1,766	54	3	45,873	10,859	24	9
50-200 m²	393	10	3	33,058	6,640	20	6
>200 m²	35	1	3	9,902	1,999	20	2

Manually labelled tree crowns from the independent test dataset are compared against the model predictions. The comparison is done for 100 random plots each 256 × 256 pixels. The statistics show the number of trees (and their crown area) that the model did not predict, for different crown size classes.

nature research

Corresponding author(s): Martin Brandt

Last updated by author(s): Jul 14, 2020

Reporting Summary

Nature Research wishes to improve the reproducibility of the work that we publish. This form provides structure for consistency and transparency in reporting. For further information on Nature Research policies, see our Editorial Policies and the Editorial Policy Checklist.

Statistics

For all statistical analyses, confirm that the following items are present in the figure legend, table legend, main text, or Methods section.

n/a	Confirmed	
☐	☒	The exact sample size (*n*) for each experimental group/condition, given as a discrete number and unit of measurement
☒	☐	A statement on whether measurements were taken from distinct samples or whether the same sample was measured repeatedly
☐	☒	The statistical test(s) used AND whether they are one- or two-sided *Only common tests should be described solely by name; describe more complex techniques in the Methods section.*
☒	☐	A description of all covariates tested
☒	☐	A description of any assumptions or corrections, such as tests of normality and adjustment for multiple comparisons
☐	☒	A full description of the statistical parameters including central tendency (e.g. means) or other basic estimates (e.g. regression coefficient) AND variation (e.g. standard deviation) or associated estimates of uncertainty (e.g. confidence intervals)
☒	☐	For null hypothesis testing, the test statistic (e.g. *F*, *t*, *r*) with confidence intervals, effect sizes, degrees of freedom and *P* value noted *Give P values as exact values whenever suitable.*
☒	☐	For Bayesian analysis, information on the choice of priors and Markov chain Monte Carlo settings
☒	☐	For hierarchical and complex designs, identification of the appropriate level for tests and full reporting of outcomes
☒	☐	Estimates of effect sizes (e.g. Cohen's *d*, Pearson's *r*), indicating how they were calculated

Our web collection on statistics for biologists contains articles on many of the points above.

Software and code

Policy information about availability of computer code

Data collection	The data were provided by DigitalGlobe within the NextView License agreement framework. There was no special software involved.
Data analysis	Only free and open source software was used for data analysis: RStudio (1.2), python (3.7), GRASS GIS (7.8), QGIS (3.10), GDAL tools (3.0). The deep learning code was written in Python (3.7) using tensorflow (2.0)

For manuscripts utilizing custom algorithms or software that are central to the research but not yet described in published literature, software must be made available to editors and reviewers. We strongly encourage code deposition in a community repository (e.g. GitHub). See the Nature Research guidelines for submitting code & software for further information.

Data

Policy information about availability of data

All manuscripts must include a data availability statement. This statement should provide the following information, where applicable:

- Accession codes, unique identifiers, or web links for publicly available datasets
- A list of figures that have associated raw data
- A description of any restrictions on data availability

Global tree cover maps are available at http://earthenginepartners.appspot.com/science-2013-global-forest. CHIRPS rainfall data is freely available at the Climate Hazard Group (http://chg.geog.ucsb.edu/data/chirps/). The Copernicus land use map can be downloaded at https://land.copernicus.eu/global/. Commercial very high resolution satellite images were acquired through the NASA under the NextView Imagery End User License Agreement (ELUA). The copyright remains at DigitalGlobe Inc. and a redistribution is not possible. However, the derived products produced by this study are made publicly available at the Oak Ridge National Laboratory at https://doi.org/10.3334/ORNLDAAC/1832. Please contact the authors for more specific requests.

Field-specific reporting

Please select the one below that is the best fit for your research. If you are not sure, read the appropriate sections before making your selection.

☐ Life sciences ☐ Behavioural & social sciences ☒ Ecological, evolutionary & environmental sciences

For a reference copy of the document with all sections, see nature.com/documents/nr-reporting-summary-flat.pdf

Ecological, evolutionary & environmental sciences study design

All studies must disclose on these points even when the disclosure is negative.

Study description	The study relies on ~11,000 satellite images at 0.5 m resolution. We applied a deep learning algorithm trained by ~90,000 manually labeled tree crowns to map 1.8 billion trees in the Sahara and Sahel region.
Research sample	The study is a wall to wall assessment of all trees and shrubs within a study area of about 1.3 million km².
Sampling strategy	No sampling was necessary as all trees and shrubs are part of the study. We have excluded trees with a crown size <3 m² as we cannot guarantee a correct mapping of this class.
Data collection	The satellite images were downloaded at NASA within the NextView license agreement from the DigitalGlobe archive and formed to moasics of 25x25 km size using the highest quality images available. The persons involved were by Katherine Melocik, Jennifer Small, CJ Tucker, Erin Glennie, Scott Sinno, Jesse Meyer, Eric Romero. Images are from the GeoEye-1, QuickBird-2, WorldView-2 and WorldView-3 satellites. All band were pansharpened to 0.5 m resolution and NDVI was calculated from the red and near infrared bands. For this study we used the panchromatic band and NDVI. GDAL tools (3.0) were used for this process.
Timing and spatial scale	The images are from November to March 2005-2018 and cover UTM zones 28 and 29 in West Africa along a rainfall gradient from 0 to 1000 mm (defined by CHIRPS v2.0 rainfall data).
Data exclusions	We only used dry season images (November to March) because this is the time where only trees have green leaves. Moreover, images with an off nadir angle >25° were not used.
Reproducibility	Data were processed twice, at Blue Waters computers and a 3xGPU workstation with the same results.
Randomization	NA, because we used all 1.8 billion trees and shrubs for the analysis without subsetting samples.
Blinding	NA, because we used all 1.8 billion trees and shrubs for the analysis without subsetting samples.

Did the study involve field work? ☒ Yes ☐ No

Field work, collection and transport

Field conditions	Field work was conducted in January 2018 and September 2016. The conditions were dry with temperatures around 30°C for both periods.
Location	The data collection was done in Senegal at Dahra in 2018 (-15.43559, 1536428) and Widou Thiengoly in 2016 (-15.31604, 15.95058).
Access & import/export	NA, because the data were noted digitally.
Disturbance	Measuring the crown size of the trees did not involve disturbances.

Reporting for specific materials, systems and methods

We require information from authors about some types of materials, experimental systems and methods used in many studies. Here, indicate whether each material, system or method listed is relevant to your study. If you are not sure if a list item applies to your research, read the appropriate section before selecting a response.

Materials & experimental systems

n/a	Involved in the study
☒	☐ Antibodies
☒	☐ Eukaryotic cell lines
☒	☐ Palaeontology and archaeology
☒	☐ Animals and other organisms
☒	☐ Human research participants
☒	☐ Clinical data
☒	☐ Dual use research of concern

Methods

n/a	Involved in the study
☒	☐ ChIP-seq
☒	☐ Flow cytometry
☒	☐ MRI-based neuroimaging